



Structurally controlled ZnO/TiO₂ heterostructures as efficient photocatalysts for hydrogen generation from water without noble metals: The role of microporous amorphous/crystalline composite structure

Siyao Guo^{a,b}, Song Han^{b,*}, Haifeng Mao^b, Shimiao Dong^b, Congcong Wu^a, Lichao Jia^a, Bo Chi^a, Jian Pu^a, Jian Li^a

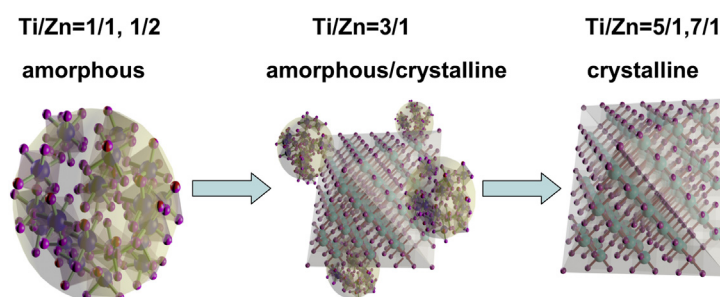
^aSchool of Materials Science and Engineering, State Key Lab of Material Processing and Die & Mould Technology, Huazhong University of Science and Technology, Wuhan 430074, China

^bCollege of Forestry, Northeast Forestry University, Harbin 150040, China

HIGHLIGHTS

- Crystalline structure controlled ZnO/TiO₂ composite catalyst.
- Amorphous/crystalline heterostructure with BET surface of 311.9 m² g⁻¹.
- The highest H₂ yield to date compared with other paper without noble metal.
- It is first report of ZnO/TiO₂ catalyst with amorphous/crystalline heterostructure.

GRAPHICAL ABSTRACT



ARTICLE INFO

Article history:

Received 28 June 2013

Accepted 8 July 2013

Available online 16 July 2013

Keywords:

Heterostructure

Amorphous/crystalline

Microporous

Hydrogen production

ABSTRACT

A versatile synthetic method, which is based on a low-temperature hydrothermal technique, is developed for the fabrication of a microporous ZnO/TiO₂ composite catalyst with different structures (e.g., amorphous, amorphous/crystalline and crystalline). In particular, a novel microporous ZnO/TiO₂ composite with amorphous/crystalline structure is obtained with a 3/1 M ratio of Ti/Zn. This novel ZnO/TiO₂ composite heterostructure not only has a large specific surface area (311.9 m² g⁻¹) but also exhibits outstanding performance during solar water splitting reactions to generate hydrogen without a noble metal co-catalyst. Based on our in-depth mechanistic analysis, the synergistic effect between the amorphous ZnO and crystalline TiO₂ is responsible for the enhanced performance of this material.

© 2013 Elsevier B.V. All rights reserved.

1. Introduction

Semiconductor photocatalysts have recently received attention because they can be widely applied to environmental purification,

solar energy conversion, and water splitting processes [1,2]. TiO₂ nanoparticles (NPs) have been extensively investigated as promising state-of-the-art photocatalysts due to their strong oxidizing power, low toxicity, low cost and facile synthesis. However, any practical improvement in the photocatalytic efficiency of TiO₂ must overcome the poor quantum yield of the catalyst, which is caused by the rapid recombination of the photogenerated electrons and holes [3]. Many attempts have been made to increase the

* Corresponding author.

E-mail address: songh77@hotmail.com (S. Han).

electron–hole pair separation efficiency and therefore improve the photocatalytic activity of TiO_2 [4–8]. Novel heterostructured inorganic nanoparticles are more active due to the improvement in their quantum yields caused by the quantum confinement effect; therefore, these types of structures are useful for applications in photocatalytic systems [9–16]. Due to their structural analogies and effective separation of photogenerated electron–hole pairs, formation of heterostructure by coupling TiO_2 with ZnO has attracted interest. Furthermore, such ZnO/ TiO_2 composites can cover a broader solar light spectrum than the pure substances, since they have different band gaps. Therefore, ZnO/ TiO_2 heterostructures are expected to exhibit better photocatalytic activity than pure TiO_2 .

Many studies have reported that amorphous materials have special properties in heterogeneous catalysis and other areas due to their novel structures and electronic characteristics. Cao et al. found that amorphous manganese oxide materials were more active as photo-oxidation catalysts than crystalline manganese oxides [17]. Yan et al. found that amorphous Fe nanoparticles have a high catalytic activity during the generation of H_2 [18]. Combining the crystalline and amorphous phases causes a synergistic effect that may improve catalytic activity and broaden the utility of these materials in many fields. For instance, Cui et al. prepared silicon crystalline/amorphous core–shell nanowires; these structures were electrochemically active and had a very high charge storage capacity when used for lithium-ion batteries [19]. Zhang et al. studied Fe@Pt core–shell NPs and found that iron in the amorphous state could promote high catalytic activity [20]. Chen et al. noted that nanocomposite $\text{Fe}_3\text{O}_4/\text{SnO}_2$ (amorphous) nanorods showed excellent microwave absorption properties [21].

Porosity, a high specific surface area and crystallinity are also crucial parameters for high performance photocatalysts; these parameters facilitate electron transfer and provide a sufficient amount of interface for photocatalytic reactions, which results in higher activity [22]. However, preparing microporous titania with a high specific surface area is difficult, and the specific surface area of most titania preparations is about $100 \text{ m}^2 \text{ g}^{-1}$ [23–26]; the specific surface area of commercial P25 is only approximately $55 \text{ m}^2 \text{ g}^{-1}$. Therefore, developing a facile route toward the synthesis of microporous titania with a large specific surface area and porosity is important.

Photocatalytic hydrogen production from water under solar irradiation is an attractive process to alleviate the global energy and environmental problems. In particular, semiconductor-based photocatalytic splitting of water to hydrogen has been become an attractive method for production of clean hydrogen energy [27–33]. However, noble metals or their oxides are widely used as surface co-catalysts in photocatalytic hydrogen generation due to their promotional effect on charge separation [34], resulting in a high catalyst. Therefore, the development of efficient photocatalysts with no scarce and costly noble metals is necessary.

A facile route, which is based on a low-temperature hydrothermal method (120°C), has been developed for the fabrication of microporous ZnO/ TiO_2 composite catalysts with different structures (amorphous, amorphous/crystalline and crystalline); structurally controlled ZnO/ TiO_2 composite NPs have been constructed through this process. To the best of our knowledge, this is the first time that ZnO/ TiO_2 composite catalysts with different crystal structures have been synthesized in a single step. Notably, this novel microporous ZnO/ TiO_2 composite, when prepared with a 3/1 M ratio of Ti/Zn, has a very large specific surface area ($311.9 \text{ m}^2 \text{ g}^{-1}$). Although some studies have been focused on TiO_2 -based heterostructures, employing amorphous ZnO to decorate crystalline TiO_2 has been rarely reported, and certainly not for heterostructures with such a high BET surface area. The new microporous ZnO/ TiO_2 composites

with an amorphous/crystalline heterostructure exhibit superior hydrogen evolution without the use of any co-catalytic noble metals. Therefore, the synthesis of these ZnO/ TiO_2 composites, which utilize ZnO in different crystal states, and the comparison of their catalytic activities are of great interest.

2. Experimental

2.1. Materials

All chemical reagents were bought from Aladdin (Shanghai, China), including tetrabutyl orthotitanate ($\text{C}_{16}\text{H}_{36}\text{O}_4\text{Ti}$, AR 99%, Aladdin), zinc acetate ($\text{Zn}(\text{CH}_3\text{COO})_2 \cdot 2\text{H}_2\text{O}$, AR 99%, Aladdin), aqueous ammonia (H_5NO , AR 25%, Aladdin) and absolute ethanol ($\text{C}_2\text{H}_6\text{O}$, AR 99.7%, Aladdin), and that were used for the synthesis of the photocatalysts and tests of the photocatalytic activity were analytical grade and used without further purification.

2.2. Catalyst preparation

Typically, 6.834 ml tetrabutyl orthotitanate was first added to 40 ml ethanol with stirring at room temperature. This is denoted Solution A. In another process, the appropriate amount of zinc acetate to achieve TiO_2/ZnO molar ratios of 1/1, 2/1, 3/1, 5/1 or 7/1 was dissolved in 20 ml deionized water with stirring, respectively. Subsequently, aqueous ammonia was cautiously added into the solution until it became transparent. This was denoted solution B. Solution B was subsequently added dropwise into solution A with vigorous stirring to form homogeneous mixture. After stirring for 2 h, the mixture was transferred to a 100 ml teflon-lined stainless steel autoclave and subjected to hydrothermal treatment at 120°C for 12 h. Finally, the powder sample was filtered, rinsed with ethanol and de-ionized water, and dried at 60°C for 12 h. Corresponding to their Ti/Zn ratios (1/1, 2/1, 3/1, 5/1 and 7/1), the samples were denoted HTZ1, HTZ2, HTZ3, HTZ5 and HTZ7.

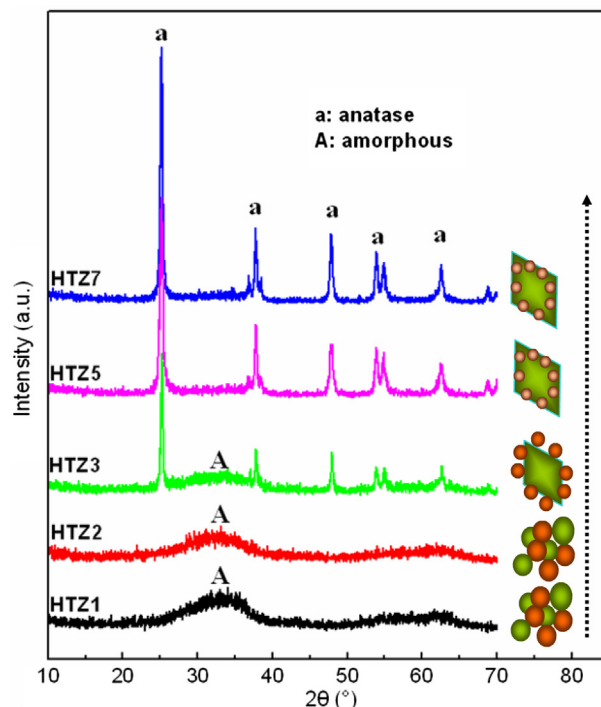


Fig. 1. XRD patterns of the prepared samples with various Ti/Zn ratios.

2.3. Photocatalytic hydrogen evolution testing

The photocatalytic H_2 evolution experiments were carried out on a LABSOLAR II (Beijing Perfectlight Technology Co. Ltd., China) photocatalytic water splitting test system with a 300 W xenon lamp, connected via a capillary tube to a mass spectrometer (Pfeiffer OmniStarT/ThermoStarT, Asslar, Germany) hydrogen detector. Typically, 10 mg samples were dispersed in 100 ml aqueous methanol solution (10 ml of methanol, 90 ml of deionized water) with magnetic stirring. A 300 W xenon lamp was employed to simulate solar light irradiation. Before irradiation, the system was pumped to remove the air, and the amount of H_2 evolved was determined with a mass spectrometer.

2.4. Characterization techniques

X-ray diffraction (XRD) patterns were collected on a Rigaku D/max-2200VPC (Tokyo, Japan) diffractometer with $CuK\alpha$ radiation operating at 40 kV and 50 mA. N_2 adsorption–desorption isotherms were recorded on a Micromeritics (Norcross, GA) ASAP

2020 surface area and porosity analyzer at liquid nitrogen temperature (77 K). The specific surface area was obtained by using the Brunauer–Emmett–Teller (BET) method, and the pore size distribution was calculated from the adsorption branch of the isotherm through a Density Functional Theory (DFT) method [35]. Transmission electron microscopy (TEM) images were obtained using a JEM (JEOL, Tokyo, Japan) field emission transmission electron microscope. To obtain crystalline structure, selected area electron diffraction (SAED) and Fourier transform (FT) of the TEM images were performed to reveal the crystalline structure. The average size was calculated by measuring the diameters of the particles in the TEM images. X-ray photoelectron spectroscopy (XPS) was performed using a Shimadzu (Toko, Japan) ESCA 750 (Mg $K\alpha$), 1253.6 eV, 240 W). The observed binding energies (BEs) were corrected by referencing the C 1s peak of the carbon contaminants at 285.0 eV. A Setaram–Labsys (Caluire, France) thermal analyzer, the samples being heated from room temperature to 1000 °C at 5 °C min^{−1}.

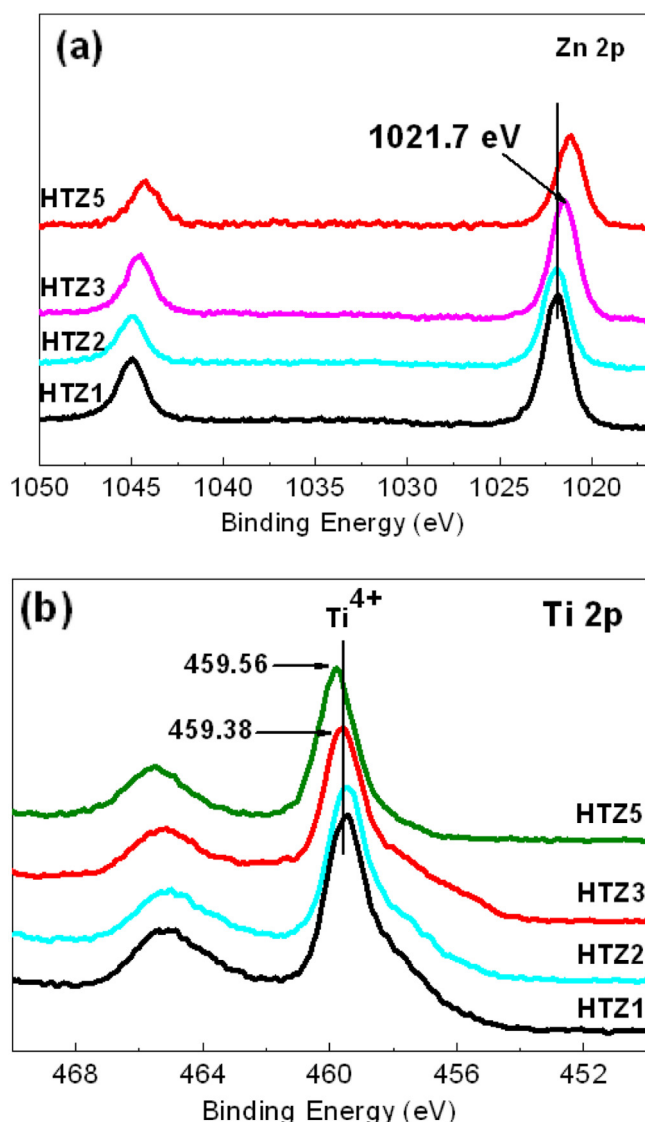


Fig. 2. XPS spectra of HTZ1, HTZ2, HTZ3 and HTZ5 (a) Zn 2p; (b) Ti 2p.

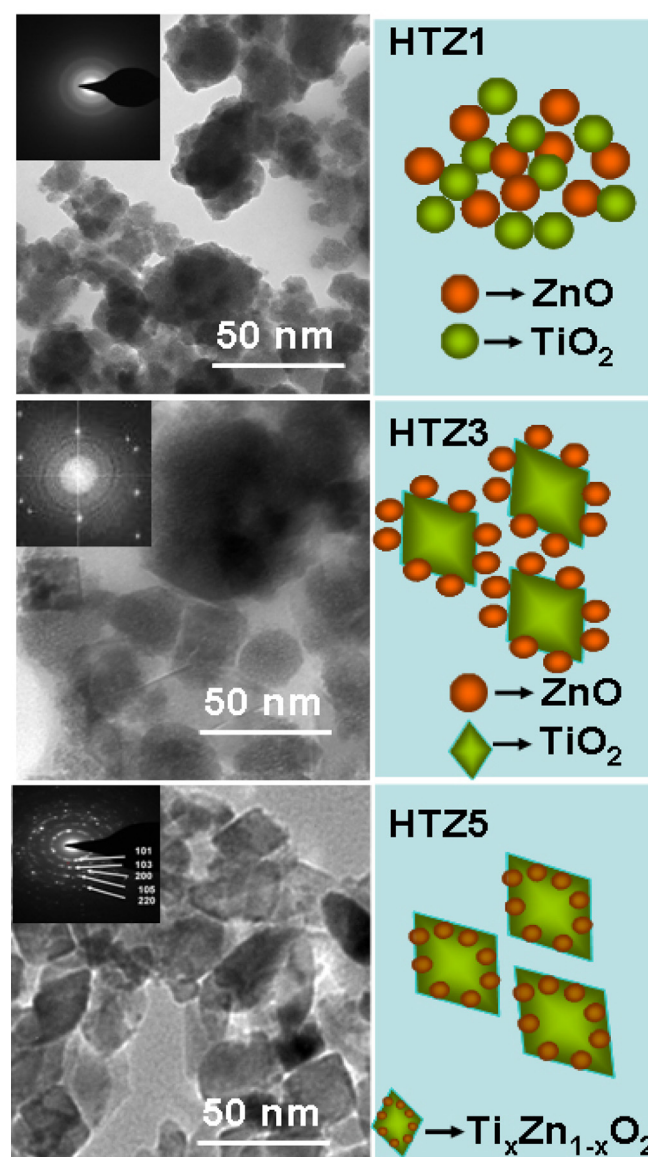


Fig. 3. TEM images for HTZ1, HTZ3 and HTZ5 samples (left). A schematic model of the crystal structure evolution for HTZ1, HTZ3 and HTZ5 (right).

3. Results and discussion

3.1. Crystal structure, morphology and porosity

The crystal structures of the ZnO/TiO₂ composites were investigated by XRD, as displayed in Fig. 1. The XRD patterns of the HTZ1 and HTZ2 samples exhibit a completely pure amorphous structure, which suggests that ZnO and TiO₂ co-exist in mixed amorphous phases. However, for HTZ3, it is interesting that there is an obviously broadened amorphous peak appearing alongside the diffraction peaks of anatase; no crystalline ZnO is present. These results suggest that the samples show higher anatase crystallinity when the TiO₂ content is increased. For the HTZ5 and HTZ7, the crystalline anatase phase can be observed, but the amorphous peak is not present; and no crystalline ZnO is visible.

To further confirm the contents of the ZnO/TiO₂ composites, depth-profiling XPS measurements were conducted to observe the interfacial interaction between ZnO and TiO₂. As displayed in Fig. 2a, the binding energies (BE) of Zn 2p_{3/2} of HTZ1, HTZ2 and HTZ3 are 1021.8, 1021.8 and 1021.7 eV, respectively, which correspond to the characteristic peak of ZnO [36]. However, there is no characteristic peak assigned to crystalline ZnO in the XRD patterns of HTZ1, HTZ2 and HTZ3. Instead, only an amorphous peak is present except for that observed for the anatase phase, implying that ZnO probably exists in amorphous form. Moreover, the BE of HTZ5 is lower than the other samples and is located at 1021.3 eV, which is attributed to the incorporation of Zn into the TiO₂ lattice [37]. Fig. 2b shows the Ti 2p peaks of HTZ1, HTZ2, HTZ3 and HTZ5 sample, which have BEs of 459.28, 459.30, 459.38, and 459.56 eV (459 eV for pure TiO₂), respectively, which correspond to Ti⁴⁺ [34]; the peak position of Ti⁴⁺ is strongly influenced by its coordination environment. Compared to the other samples, the BE of HTZ5 shows a positive shift compared with the that of the Zn 2p, which results from the lattice doping of Zn²⁺ into TiO₂ lattice with the formation of Ti–O–Zn bonds. This is because the electronegativity difference between Zn and Ti (Zn > Ti) will give a partial electron transfer from Ti to O, resulting in lower electron density of the Ti ion. Therefore, combined with the above XRD result, it is inferred that the crystal structure of the ZnO/TiO₂ composites experience an amorphous, amorphous/crystalline and crystalline transition process with increasing TiO₂ ratio, which is confirmed by the following TEM analysis.

Fig. 3 (left) displays the TEM images of HTZ1, HTZ3, and HTZ5 samples, respectively. It is found that HTZ1 has an irregular shape with particle size less than 100 nm. The inset SAED result confirms that the HTZ1 sample is composed entirely of amorphous particles, which is consistent with the XRD analysis. The inset FT result confirms that both amorphous and crystalline phases co-exist when the Ti/Zn ratio reaches 3/1 (HTZ3) (for technical reasons concerning the TEM, we used a FT image instead of a SAED image). Based on the above XRD and XPS analyses, we deduce that the amorphous phase is mainly composed of ZnO surrounding the crystalline TiO₂, giving an amorphous/crystalline ZnO/TiO₂ heterostructure. When the Ti/Zn ratio increases to 5/1 (HTZ5), no amorphous phase is present in the TEM or SAED pattern, and only pure anatase nanocrystals that are approximately 30–40 nm can be observed, which is consistent with the XRD result. The SAED result also suggests the existence of the crystalline anatase with d_{hkl} values of 0.351 nm, 0.243 nm, 0.189 nm, 0.170 nm and 0.133 nm, which correspond to the (101), (103), (200), (105) and (220) planes indexed to hexagonal TiO₂ (JCPDS 21-1272).

Based on the TEM images, a schematic model of the evolution of the crystal structure of HTZ1, HTZ3, and HTZ5 samples is shown in Fig. 3 (right). First, the ZnO/TiO₂ composite shows pure completely amorphous structure when the Ti/Zn ratio is 1/1. Subsequently, when the TiO₂ content increases, the ZnO/TiO₂ composite, which consists of crystalline TiO₂ that is decorated with amorphous ZnO, appears when the Ti/Zn ratio reaches 3/1. When the Ti/Zn ratio is 5/1, the composite catalyst shows a pure anatase phase according to the XRD results; Zn may replace Ti to form Zn-doped TiO₂ (Ti(Zn)O₂), based on the XPS analysis. Therefore, it can be inferred that the molar ratio of Ti/Zn plays an important role because it must determine the crystalline structure of the ZnO/TiO₂ heterostructure.

Fig. 4a shows an HRTEM image of HTZ3. The lattice fringe of HTZ3 is clearly observed, showing the existence of the crystalline of TiO₂. The lattice spacing (0.351 nm) corresponds to the anatase (101) planes, indicating that the crystal growth is preferential along the [101] direction. Moreover, the low intensity points on the HRTEM image support the presence of a large number of crystalline defects in the HTZ3 crystalline structure. The corresponding filtered image clearly demonstrates how the crystal planes are interrupted by the extensive defects in its structure [38]. The presence of these

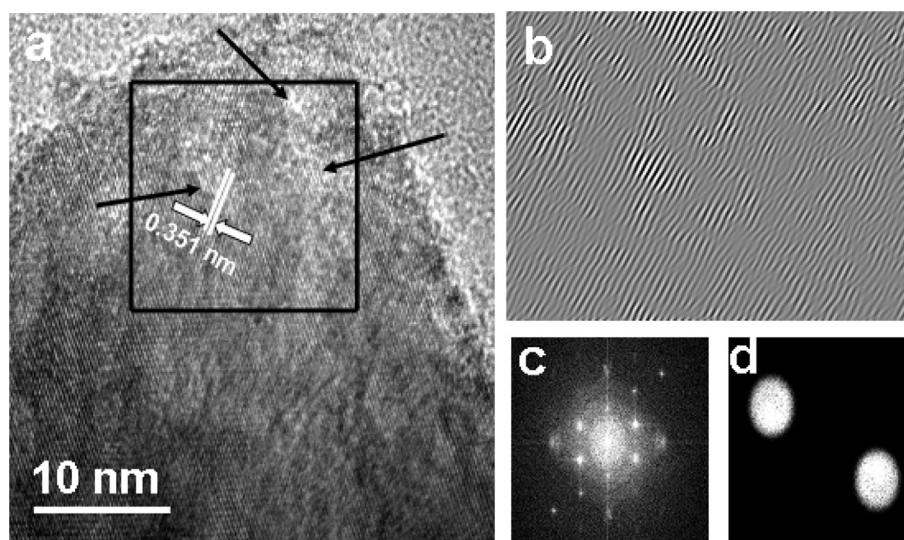


Fig. 4. (a) HRTEM image of HTZ3 nanoparticles. The arrows point to the defects. (b) Filtered image from the square area in (a) including the spots of 0.351 nm (c) FT of the square area in (a). (d) Mask used to reconstruct the image (b).

lattice defects in the HTZ3 composite may generate distinct effects that mediate the electronic structure or tune the atomic arrangement; these defects could be beneficial for improving its photocatalytic activity.

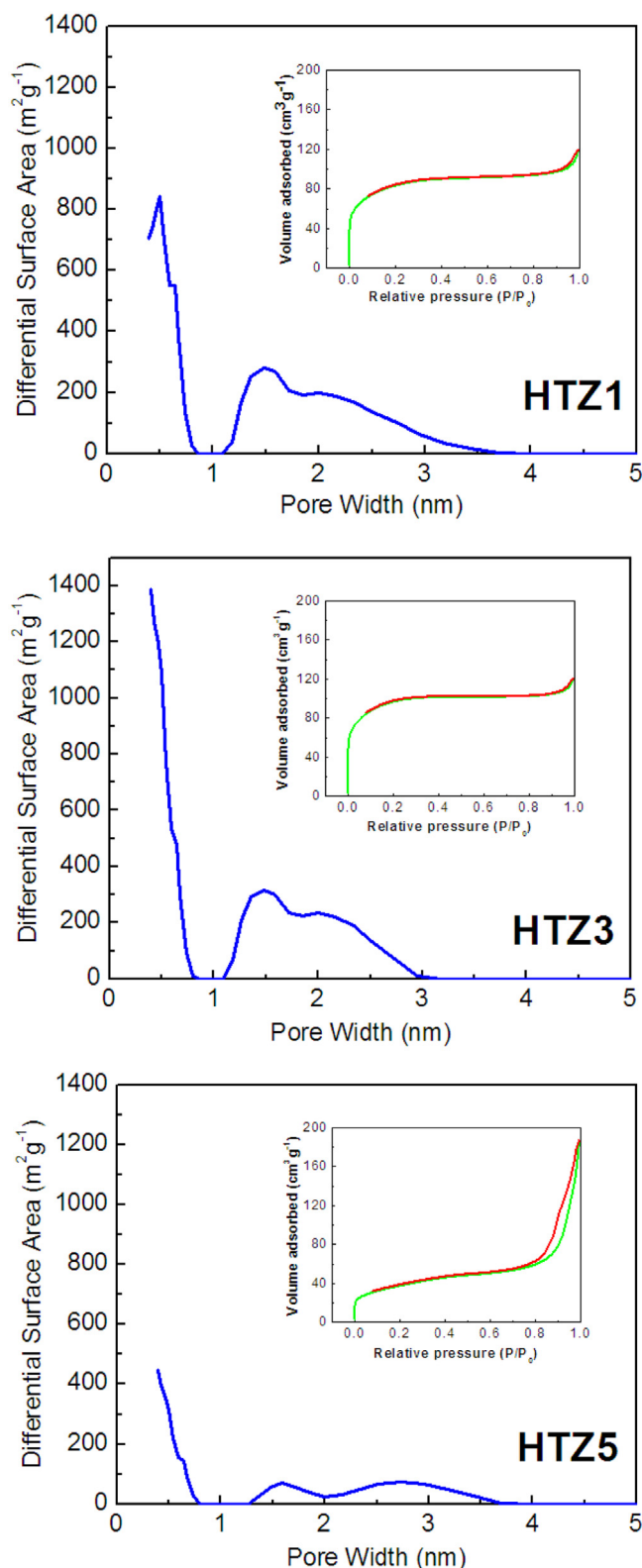


Fig. 5. Pore size distributions for HTZ1, HTZ3 and HTZ5 employing the DFT method. N_2 adsorption isotherms are shown in their respective insets.

The N_2 adsorption/desorption isotherms of the HTZ1, HTZ3 and HTZ5 samples are displayed in Fig. 5. Clearly, those of HTZ1 and HTZ3 may be classified as typical type I isotherms characteristic of microporous materials. The N_2 adsorption volume of HTZ3 is higher than that of HTZ1, which indicates that HTZ3 has a higher microporous area (approximately 70% of the total pore surface area). The isotherms of HTZ5 are type IV isotherms, indicating the presence of well-developed mesoporosity in the sample. The specific surface areas of each sample, which were calculated by the multi-point Brunauer–Emmett–Teller (BET) method, are $272.4 \text{ m}^2 \text{ g}^{-1}$, $311.9 \text{ m}^2 \text{ g}^{-1}$ and $130.1 \text{ m}^2 \text{ g}^{-1}$ for HTZ1, HTZ3 and HTZ5, respectively. The above analysis validates the pore size distributions obtained using the DFT method [35]. Therefore, the sample with amorphous/crystalline heterostructure is easily formed microporous structure, resulting in a high specific surface area. The BET surface area, micropore area, pore size and pore volume are summarized in Table 1.

3.2. TG/DTA analysis

The experimental TG/DTA curves are shown in Fig. 6. The TG diagrams of HTZ1, HTZ3 and HTZ5 may be divided into two main stages. The first one occurs in the range of $40\text{--}320^\circ\text{C}$; the total weight loss, which was about 25%, which is due to the evaporation of the physically adsorbed water ($30\text{--}130^\circ\text{C}$) and the loss of chemically adsorbed water ($140\text{--}310^\circ\text{C}$). The second one, which was in the range of $320\text{--}500^\circ\text{C}$, is a weight loss of 5%, may be mainly attributed to oxy-hydroxide decomposition. It is observed that the weight loss for HTZ1 and HTZ3 is much larger than that for HTZ5. The large quantity of micropores in HTZ1 and HTZ3 can promote the adsorption of more water, resulting in more weight loss during TG/DTA analysis. Correspondingly, the endothermic reaction peaks for HTZ1, HTZ3 and HTZ5 in the DTA curves at approximately 70°C are due to the evaporation of water. There is no endothermic or exothermic peak from 300°C to 700°C . Normally, anatase TiO_2 will transform to rutile in the $500\text{--}700^\circ\text{C}$ temperature range. These results indicate that the presence of ZnO will benefit the stability of anatase TiO_2 .

3.3. Photocatalytic activity

Fig. 7a displays the time curve for photocatalytic H_2 production over the ZnO/ TiO_2 composite catalyst, which has with different Ti/Zn ratios, without any noble metal under xenon lamp irradiation. A significant increase in the H_2 evolution rate can be observed after 1 h, which suggests the occurrence of light-induced surface activation. HTZ3 (amorphous/crystallite structure) shows the highest H_2 yield ($6918 \mu\text{mol}$ of H_2) compared to HTZ1 (pure amorphous), HTZ5 and HTZ7 (pure crystalline) under xenon lamp irradiation. Fig. 7b shows the rates of H_2 evolution. Clearly, HTZ3 shows the highest average H_2 yield ($865 \mu\text{mol h}^{-1} \text{ g}^{-1}$) compared with those of the other samples, while HTZ1 shows the lowest at $296 \mu\text{mol h}^{-1} \text{ g}^{-1}$. The results therefore show that composites with

Table 1
Summary of the physicochemical properties of HTZ1, HTZ3 and HTZ5.

Samples	BET ^a ($\text{m}^2 \text{ g}^{-1}$)	Micropore area ^b ($\text{m}^2 \text{ g}^{-1}$)	Pore size ^c (nm)	Pore volume ^d ($\text{cm}^3 \text{ g}^{-1}$)
HTZ1	272.4	105.9	2.7	0.18
HTZ3	311.9	143.3	2.3	0.19
HTZ5	130.1	13.6	8.7	0.29

^a Determined by applying Brunauer–Emmett–Teller (BET) equation.

^b T-Plot micropore area.

^c Adsorption average pore width ($4V/A$ by BET).

^d Single point adsorption total pore volume of pores at $P/P_0 = 0.99$.

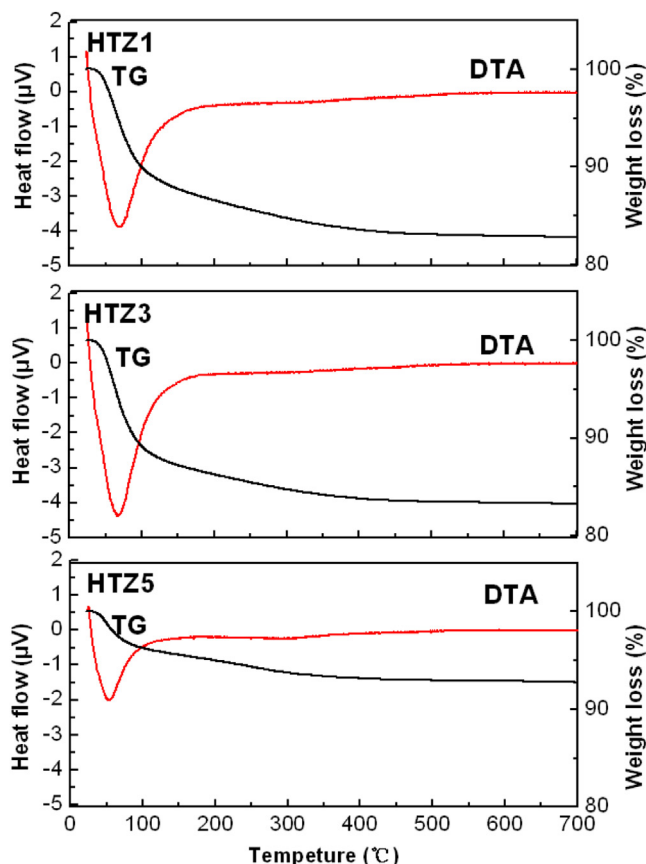


Fig. 6. TG–DTA curves for HTZ1, HTZ3, and HTZ5 samples heated from room temperature to 800 °C in air.

an amorphous/crystalline structure have better photocatalytic performance than those with completely amorphous or crystalline phases.

3.4. Mechanistic analysis

Based on the above photocatalytic test, HTZ1 and HTZ2 with full amorphous structure show lower photocatalytic activity than other samples, even though they also have large specific surface area, indicating that amorphous structure alone does not effectively improve performance. A similar result has also been reported by Ohtani et al., who show that amorphous phase material usually shows poor catalytic activity [39], which is consistent with the present work. Though the photocatalytic activity of HTZ5 and HTZ7 (pure crystalline nanoparticles) is slightly better than that of HTZ1 (pure amorphous), their performance is still lower than that of HTZ3, which has an amorphous/crystalline structure. The latter can give result in distinct mediating of the electronic structure or tuning the atomic arrangement and will generate a high concentration of unsaturated sites, which renders easier adsorption and more rapid surface reactions than on purely crystalline catalysts [40]. In particular, the synergistic effect that results from the combination of crystalline and amorphous generates highly active catalytic centers, which facilitates the improvement of the photocatalytic performance. Similarly, Bickley and co-workers have reported that Degussa P25 consisting of the amorphous state together with crystalline anatase and rutile showed unusually high photocatalytic activity, which was attributed to the complex structure and the localized Anderson states of amorphous TiO_2 ,

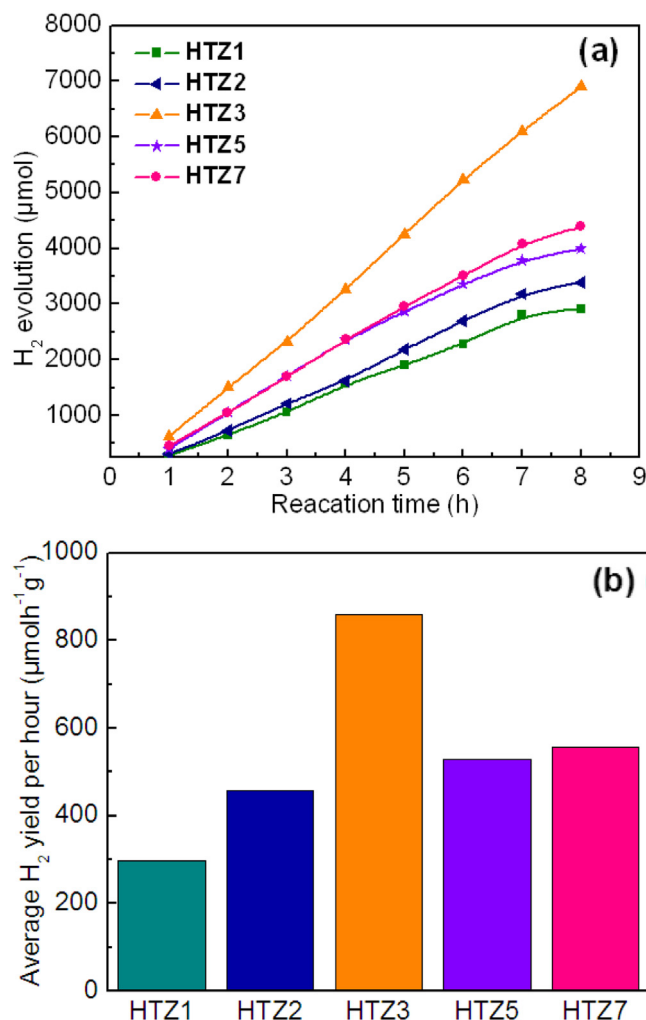


Fig. 7. Photocatalytic activity of ZnO/TiO_2 composite catalysts with different Ti/Zn ratio for hydrogen production from water in the absence of noble metal under xenon lamp irradiation: (a) time curve of photocatalytic hydrogen production (b) the rates of hydrogen evolution.

these parameters may increase the lifetimes of the electrons/holes pairs and thereby enhance the photocatalytic activity [41].

In addition to the benefits of the amorphous/crystalline composite structure mentioned above, the intrinsic advantages of the ZnO/TiO_2 heterostructure also play an important role in the separation of the photogenerated electron–hole pairs. Fig. 8 shows a configuration model of HTZ3, which consists of crystalline TiO_2 with amorphous ZnO . The high activity of the composite photocatalyst is attributed to the occurrence of fast charge separation. The different positions of the conduction bands from the ZnO and TiO_2 drives the photoelectrons on the ZnO to the TiO_2 nanoparticles immediately upon light absorption, therefore forcibly separating the pairs of electrons/holes on the surface and reducing their recombination; this effect enhances the photocatalytic activity of the catalyst. In contrast to crystalline ZnO , the decorated amorphous ZnO makes intimate contact with the TiO_2 by forming a heterostructure, which results in more facile charge transfer and better separation efficiency. Moreover, HTZ3, which has an amorphous/crystalline composite structure, also possesses a large specific surface area ($311.9 \text{ m}^2 \text{ g}^{-1}$), which provides a large interface for photocatalytic reaction. Therefore, the homogeneous distribution of amorphous ZnO and the enlarged specific surface areas are

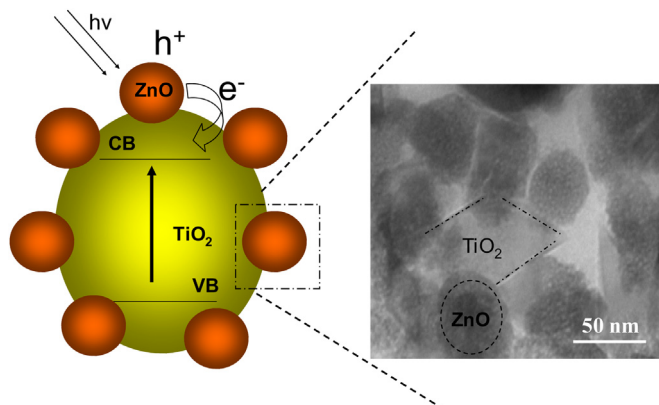


Fig. 8. A configuration model of HTZ3 consisting of crystalline TiO_2 with amorphous ZnO. A TEM image of the interface between crystalline TiO_2 and amorphous ZnO is also shown.

beneficial in improving the photocatalytic activity. Furthermore, as confirmed by HRTEM analysis, the large number of lattice defects on the surface of the amorphous/crystallite composite structure also provides more active sites for photocatalytic reaction, which favors improved photocatalytic activity. Therefore, an enhanced catalytic effect may be expected for catalysts composed of a mixture of amorphous and crystalline structure.

4. Conclusions

In summary, structurally controlled ZnO/TiO_2 composite photocatalysts have been successfully synthesized via a low-temperature hydrothermal method (120 °C). By adjusting the Ti/Zn ratio, ZnO/TiO_2 composite photocatalysts with different amorphous, amorphous/crystalline and crystalline structures may be obtained. In particular, a novel microporous ZnO/TiO_2 composite with an amorphous/crystalline structure is obtained when the Ti/Zn ratio is 3/1 and possesses a large specific surface area, which is $311.9 \text{ m}^2 \text{ g}^{-1}$. With no noble metal co-catalyst, this novel ZnO/TiO_2 heterostructure shows enhanced H_2 evolution ($865 \mu\text{mol h}^{-1} \text{ g}^{-1}$) under xenon lamp irradiation; $6918 \mu\text{mol}$ of H_2 are collected after 8 h of irradiation. The enhanced photocatalytic activity is attributed to the synergy between the crystalline TiO_2 and the amorphous ZnO. These results confirm that amorphous state ZnO is a distinct and powerful catalytic center for TiO_2 -based composite catalysts. The resultant amorphous/crystallite ZnO/TiO_2 heterostructure exhibits high catalytic activity, low cost, long-term stability, and ease of recovery, with the potential as a high performance photocatalyst.

Acknowledgments

The work is supported by the Fundamental Research Funds for the Central Universities (DL11EB02), the New Century Excellent Talents in University (NCET-10-0277), the Ministry of Transportation (2009318000088) and the National Natural Science Foundation of China (21176047). The authors would like to thank

the Materials Characterization Center of Huazhong University of Science and Technology for assistance with the measurement of the samples.

References

- [1] A. Fujishima, K. Honda, *Nature* 238 (1972) 37–38.
- [2] K. Lee, D. Kim, P. Roy, I. Paramasivam, B.I. Birajdar, E. Spiecker, P. Schmuki, *J. Am. Chem. Soc.* 132 (2010) 1478–1479.
- [3] Z. Song, Q. Li, *J. Mater. Sci. Technol.* 13 (1997) 321–323.
- [4] J. Wang, D.N. Tafen, J.P. Lewis, Z.L. Hong, A. Manivannan, M.J. Zhi, M. Li, N.Q. Wu, *J. Am. Chem. Soc.* 131 (2009) 12290–12297.
- [5] S.Y. Guo, S. Han, H.F. Mao, C.C. Wu, L.C. Jia, B. Chi, J. Pu, J. Li, *J. Alloys Compd.* 544 (2012) 50–54.
- [6] L.X. Yang, S.L. Luo, Y. Li, Y. Xiao, Q. Kang, Q.Y. Cai, *Environ. Sci. Technol.* 44 (2010) 7641–7646.
- [7] S.Y. Guo, S. Han, H.F. Mao, C.H. Zeng, Y. Sun, B. Chi, J. Pu, J. Li, *Mater. Res. Bull.* (2013), <http://dx.doi.org/10.1016/j.materresbull.2013.04.056>.
- [8] S. Kim, B. Fisher, H.J. Eisler, M. Bawendi, *J. Am. Chem. Soc.* 125 (2003) 11466–11467.
- [9] I. Lee, J.B. Joo, Y.D. Yin, F. Zaera, *Angew. Chem. Int. Ed.* 50 (2011) 10208–10211.
- [10] Y.H. Zhou, X.Y. Li, X.L. Pan, X.H. Bao, *J. Mater. Chem.* 22 (2012) 14155–14159.
- [11] X.W. Wang, G. Liu, G.Q. Lu, H.M. Cheng, *Int. J. Hydrogen Energy* 35 (2010) 8199–8205.
- [12] Y. Huo, X. Yang, J. Zhu, H. Li, *Appl. Catal. B Environ.* 106 (2011) 69–75.
- [13] R. Ciancio, E. Carlino, C. Aruta, D. Maccariello, F.M. Granozio, U.S.D. Uccio, *Nanoscale* 4 (2012) 91–94.
- [14] J.S. Chen, D.Y. Luan, C.M. Li, F.Y.C. Boey, S.Z. Qiao, X.W. Lou, *Chem. Commun.* 46 (2010) 8252–8254.
- [15] I.L. Hsiao, Y.J. Huang, *Chem. Res. Toxicol.* 24 (2011) 303.
- [16] J.S. Jang, H.G. Kim, P.H. Borse, J.S. Lee, *Int. J. Hydrogen Energy* 32 (2007) 4786–4791.
- [17] H. Cao, S.L. Sui, *J. Am. Chem. Soc.* 116 (1994) 5334–5342.
- [18] J.M. Yan, X.B. Zhang, S. Han, H. Shioyama, Q. Xu, *Angew. Chem. Int. Ed.* 47 (2008) 2287–2289.
- [19] L.F. Cui, R. Ruffo, C.K. Chan, H.L. Peng, Y. Cui, *Nano Lett.* 9 (2009) 491–495.
- [20] X.B. Zhang, J.M. Yan, S. Han, H. Shioyama, Q. Xu, *J. Am. Chem. Soc.* 131 (2009) 2778–2779.
- [21] Y.J. Chen, P. Gao, R.X. Wang, C.L. Zhu, L.J. Wang, M.S. Cao, H.B. Jin, *J. Phys. Chem. C* 113 (2009) 10061–10064.
- [22] A.A. Ismail, D.W. Bahnemann, *J. Mater. Chem.* 21 (2011) 11686–11707.
- [23] C. Jin, R.Y. Zheng, Y. Guo, J.L. Xie, Y.X. Zhu, Y.C. Xie, *J. Mol. Catal. A Chem.* 313 (2009) 44–48.
- [24] P. Kubiak, T. Froeschl, N. Huesing, U. Hoermann, U. Kaiser, R. Schiller, C.K. Weiss, K. Landfester, M. Wohlfahrt-Mehrens, *Small* 7 (2011) 1690–1696.
- [25] L.H. Chang, N. Sasirekha, Y.W. Chen, *Catal. Commun.* 8 (2007) 1702–1710.
- [26] A. Beck, G. Magesh, B. Kuppam, Z. Schay, O. Geszti, T. Benko, R.P. Viswanath, P. Selvam, B. Viswanathan, L. Gucci, *Catal. Today* 164 (2011) 325–331.
- [27] Y.H. Pai, C.T. Tsai, S.Y. Fang, *J. Power Sources* 223 (2013) 107–113.
- [28] B. Naik, S. Martha, K.M. Parida, *Int. J. Hydrogen Energy* 36 (2011) 2794–2802.
- [29] N. Strataki, M. Antoniadou, V. Dracopoulos, P. Lianos, *Catal. Today* 151 (2010) 53–57.
- [30] T. Sreethawonga, C. Junbua, S. Chavadej, *J. Power Sources* 190 (2009) 513–524.
- [31] Y.L. Liu, L.J. Guo, W. Yan, H.T. Liu, *J. Power Sources* 159 (2006) 1300–1304.
- [32] Z.W. Seh, S.H. Liu, M. Low, S.Y. Zhang, Z.L. Liu, A. Mlayah, M.Y. Han, *Adv. Mater.* 24 (2012) 2310–2314.
- [33] H.H. Yang, L.J. Guo, W. Yan, H.T. Liu, *J. Power Sources* 159 (2006) 1305–1309.
- [34] T. Sreethawong, S. Laehsatee, S. Chavadej, *Catal. Commun.* 10 (2009) 538–543.
- [35] C. Lastoskie, K.E. Gubbins, N. Quirke, *J. Phys. Chem.* 97 (1992) 4786–4796.
- [36] M.T. Tsai, Y.U. Chang, H.L. Huang, J.T. Hsu, Y.C. Chen, A.Y.J. Wu, *Thin Solid Films* 528 (2013) 143–150.
- [37] L. Ramquist, K. Hamrin, G. Johansson, A. Fahlmann, C. Nording, *J. Phys. Chem. Solids* 30 (1969) 1835–1847.
- [38] M. Boutinguiza1, B. Rodriguez-Gonzalez, J.D. Val, R. Comesana1, F. Lusquinos, *J. Pou1, Nanotechnology* 22 (2011) 195606.
- [39] B. Ohtani, Y. Ofawa, S.I. Nishimoto, *J. Phys. Chem. B* 101 (1997) 3746–3752.
- [40] J.F. Deng, H.X. Li, W.J. Wang, *Catal. Today* 51 (1999) 113–125.
- [41] R.I. Bickley, T. Gonzalez-Carreno, J.S. Lees, *J. Solid State Chem.* 92 (1991) 178–190.